International Journal of Mathematical, Engineering and Management Sciences
Vol. 11, No. 2, 753-774, 2026
https://doi.org/10.33889/IJMEMS.2026.11.2.031

A Fuzzy-Based Computational Framework for MHD Sutterby Hybrid Nanofluid Flow with Bioconvection Induced by Microorganism and Homogeneous–Heterogeneous Chemical Reaction

M. Perumalsamy
Department of Mathematics,
Government College of Technology, Coimbatore, Tamil Nadu, India.
E-mail: perumalsamy@gct.ac.in

P. Asaigeethan
Department of Mathematics,
Government College of Engineering, Erode, Tamil Nadu, India.
Corresponding author: asaigeethan14@gct.ac.in

M. Gnana Kumar
Department of Mathematics,
Government College of Technology, Coimbatore, Tamil Nadu, India.
E-mail: gnanakumar@gct.ac.in

J. Duraikannan
Department of Mathematics,
Government College of Technology, Coimbatore, Tamil Nadu, India.
E-mail: jduraikannan@gct.ac.in

N. Deepa
Department of Mathematics,
Government College of Technology, Coimbatore, Tamil Nadu, India.
E-mail: dheepimath@gct.ac.in

(Received on September 16, 2025; Revised on December 17, 2025; Accepted on February 20, 2026)

Abstract
This research work studied the magnetohydrodynamic (MHD) Sutterby hybrid nanofluid flow over a stretching sheet, incorporating thermal radiation along with homogeneous and heterogeneous chemical reactions (H-H), while the modified Buongiorno's model utilizes significant scientific facts to represent the complex behavior of nanofluids. Cadmium selenide ($CdSe$) and chitosan $(C_6H_{11}NO_4)_n$ are used to generate hybrid nanoparticles that block greater solar thermal radiation. This could improve radiative shielding by 25 to 30% compared to typical single-phase sunscreen formulas. Utilized MATLAB's bvp5c solver to find out that raising the Deborah number makes the velocity go up by 22 to 28%, but increasing the magnetic parameter makes it go down by 20 to 35% because of Lorentz damping. Nonlinear radiation raises the temperature field by 18 to 24%, and greater Schmidt numbers lower concentration levels by roughly 30%. Bioconvection research shows that the Peclet number increases the density gradients of microorganisms by 12 to 18%, which makes it easier for germs to migrate up. However, higher bioconvective Lewis numbers make motile-cell diffusion 10 to 15% lower. This demonstrates the sensitivity of mass diffusion to nanoparticle interactions. In fuzzy set theory (FST), the derived triangular fuzzy numbers (TFNs) are employed to represent uncertainty in the volume percentage of nanoparticles within the range [0, 0.05, 0.1]. The fuzzy velocity profiles that come out of these calculations reveal an 8 to 12% variance from the clear answer. The fuzzy midpoint has the highest flow rate. These findings indicate that uncertainty in nanoparticle loading significantly influences heat and momentum transfer.

Keywords- Sutterby hybrid nanofluid, Thermal radiation, H-H, microorganism, Triangular membership functions, TFN, FST.

Nomenclatures

D_e	Deborah parameter	θ_w	Temperature-ratio parameter
Re	Reynolds parameter	ω	Microorganism difference number
B_0	Magnetic field parameter	θ	Dimensionless temperature
λ	velocity ratio	ρ	Fluid density (kgm^{-3})
Rd	Radiation parameter	η	Dimensionless similarity variable
Pr	Prandtl number	C_p	Specific heat capacity ($Jkg^{-1}K^{-1}$)
Lb	Lewis number	κ	Thermal conductivity ($Wm^{-1}K^{-1}$)
Pe	Peclet number	σ	Electrical conductivity ($\Omega^{-1}\ cm^{-1}$)
x, y	Surface coordinate system (m)	φ_1, φ_2	Nanoparticle volume fractions
Sc	Schmidt number	ν	Kinematic viscosity(m^2/s)
Ls	H-H parameter	α	Thermal diffusivity(m^2/s)
Nb	Brownian motion parameter	m, n	Nanoparticle concentrations (mol/m^3)
Nt	Thermophoretic diffusion parameter	D_A, D_B	Brownian diffusion coefficients (m^2/s)
n	Power law index number	nf	Nanofluid - $CdSe/Blood$
D_M	Microorganism diffusion constant	hnf	Hybrid nanofluid - $CdSe + (C_6H_{11}NO_4)_n/Blood$
Nu	Nusselt parameter		

1. Introduction

MHD non-Newtonian fluid flow models are essential for the complex transportation occurrences that are present in biomedical engineering, industrial engineering, etc. The Sutterby fluid model accurately describes high-polymer solutions and other complex fluids, apprehends the constant power law index number (n) manners, and characterizes Newtonian fluids. Incorporating some nanoparticles into Sutterby fluid can produce improved transfer of heat and mass. The dynamics of some fluid parameters increase the fluid flow in 2D/3D geometry. The MHD Sutterby hybrid nanofluid systems are particularly beneficial for biomedical transport effects. Explained 2D non-Newtonian Sutterby hybrid nanofluid flows over a parabolic surface. In the boundary layer, surface buoyancy-driven flow occurs because the reaction between the Sutterby hybrid nanofluid and the catalyst at the surface creates big temperature differences (Basit et al., 2023). Used the Cattaneo-Christov system for heat flux to look into how thermal radiation and inclined magnetic fields affect the Sutterby fluid (Sabir et al., 2021). Analyzed the inalterability in Sutterby nanofluid flow caused by a stretched cylinder. The velocity equation is described by porosity, Darcy-Forchheimer, and the magnetic field parameter. The temperature equation takes into consideration the effects of thermal radiation and Joule heating (Rahman et al., 2023). Explained the fluid flow and temperature transfer characteristics of a blood-based fluid composite nanoparticle, which consists of Sutterby hybrid fluid over a bi-directional porous stretching sheet (Khan et al., 2023). An analysis of the boundary layer is dispensed for mixed convection occurring past a vertical wedge within a porous medium saturated with a nanofluid (Gorla et al., 2010). Examined the endorsed thermal aspect of Sutterby nanofluid that contains microorganisms due to a stretched cylinder. Also included in the thermal perspective are nonlinear thermal radiation, Darcy resistance, and activation energy (Aldabesh et al., 2022). The depicted 2D non-Newtonian Casson nanofluid flow on the upper horizontal surface of a parabola is examined. The effects of catalytic surface chemical reactions are considered (Zeeshan et al., 2021). The study examines the properties of bioconvective MHD flow with suspended hybrid nanoparticles traversing an expanding porous substrate (Farooq et al., 2024). Examined the present mathematical model developed to the results of bioconvective cross-diffusion fluid flow of a magnetized viscous nanofluid flow in cones, wedges, and plates with convective boundary conditions. (Khan et al., 2021). Illustrating the movement of the nanofluids can effectively control the enhanced heat transfer that results from stretching sheets. The issues of nanoparticle concentration, settling in the viscous MHD fluid, and bioconvection are addressed (Asjad et al., 2022). This study explored the characteristics of bio-convection in Casson nanofluid, which incorporates thermal radiation and activation energy, beyond a horizontal paraboloid region (Imran et al., 2022). Studied the effects of bioconvection on Williamson

nanofluid flow, including the nonlinear heat radiation and chemical reaction influences on stretching sheets (Awan et al., 2022). The study focused on the stable biomagnetic hybrid nanofluid (HNF) of oxytactic microorganisms moving through a slender needle in a magnetic field, using the adapted Buongiorno's nanoliquid model (Ramesh et al., 2022). The study explores the heat transfer phenomena of MHD nanofluid over a moving vertical plate, focusing on the interaction with thermal radiation (Dash et al., 2022). Examines the significant influence of entropy generation and activation energy on the dynamics of hydromagnetic nanofluids, emphasizing nonlinear thermal radiation, viscous and Ohmic dissipation, and Hall current effects on a linear stretching sheet (Mondal and Pal, 2024). Investigates the impact of H-H reactions on peristaltic flow through an inclined permeable channel, focusing on the modelling of blood flow in narrow arteries by considering convective and wall properties (Vaidya et al., 2021). Examined the magnetic Sisko fluid flow through a stretching sheet under convective conditions utilizing Buongiorno's model and the flow issue arising from H-H reactions (Upreti et al., 2022). Examined the dynamics of 3D nanofluid flows influenced by MHD, the Darcy-Forchheimer law, bioconvection of motile microorganisms, nonlinear thermal radiation, and activation energy (Hamid et al., 2025). This study investigates the unstable flow at the stagnation point of a hybrid nanofluid in the boundary layer as it interacts with a permeable sheet that contains nanoparticles and gyrotactic bacteria. This finding has significant potential applications in bioconvection, which is critical to ecological and biotechnological processes (Mohamed et al., 2025).

FST models exhibit greater uncertainty compared to crisp assumptions in fluid flow studies. Triangular membership functions (TMF) assume fuzzy boundary conditions and governing parameters in these systems. Fluid mechanics models can use faulty variables according to Zadeh's extension approach (Barhoi et al., 2018). Studied fuzzy hybrid nanofluid models and found that TFN-based uncertainty modelling does a competent job of capturing imprecision in volume fractions for both analytical and numerical research (Zulqarnain et al., 2023). Researchers have also looked into how nanofluids behave when they are in uncertain surroundings by looking at fuzzy volume fractions and triangular fuzzy numbers (Biswal et al., 2020). Foundational contributions delineating triangular, Gaussian, and trapezoidal fuzzy numbers have facilitated these advancements (Dubois and Prade, 1978), whereas the theoretical construct of fuzzy derivatives has further fortified fuzzy-based analytical modelling (Seikkala, 1987).

Most previous research examined specific impacts like MHD flow, radiation, bioconvection or hybrid nanofluid heat transfer independently. In contrast, the current work uniquely incorporates hybrid nanoparticles, nonlinear radiation, homogeneous-heterogeneous reactions, slip conditions, microorganism dynamics and fuzzy uncertainty in one model, providing a more detailed analysis than previous studies. This study aims to determine how hybrid nanoparticles can improve thermal protection in extreme solar radiation conditions. Hybrid nanofluids can reduce radiative heat transfer to sensitive surfaces by enhancing working fluid absorption and scattering, making them beneficial in thermal-management and protective-coating applications. The model analyses hybrid nanomaterial properties using modified Buongiorno's nanofluid framework in two parts. The first part is heat transfer while accounting for thermal radiation, Joule heating, viscous dissipation, Brownian motion and thermophoretic effects. The second component accounts for nanoparticle volume fraction uncertainty using fuzzy differential equations (FDEs). The α-cut method and triangular fuzzy numbers (TFNs) are used to describe imprecise nanoparticle concentrations, with the membership function defining the uncertainty range.

This model has practical applications in solar-thermal protection systems and biomedical cooling applications, such as nanoparticles ($CdSe$ and $(C_6H_{11}NO_4)_n$) and blood-mediated heat regulation under strong radiation exposure, because it examines the combined effects of MHD control, nonlinear thermal

radiation, homogeneous–heterogeneous chemical reactions, bioconvection, and fuzzy uncertainty modelling. The approach also applies to magnetically controlled nanofluid cooling devices, catalytic reactors and microfluidic biomedical systems, where uncertainty about the concentration of nanoparticles and complicated transport mechanisms is very important.

The novelty of this research work is defined as follows:

- The simultaneous incorporation of MHD flow, nonlinear thermal radiation, homogeneous-heterogeneous chemical reactions, and bioconvection induced by motile microorganisms and non-Newtonian Sutterby hybrid nanofluid dynamics into an integrated mathematical framework.
- This study involves the integration of a fuzzy-based computational methodology that employs triangular fuzzy numbers and the $\alpha - cut$ technique to represent uncertainty in nanoparticle volume fraction, a subject that has not been examined in a unified manner in previous research.
- A direct comparison with existing literature demonstrates that most previous studies have examined these impacts individually or partially, whereas the current study addresses them within an integrated and consistent framework.

2. Fuzzy Concept

Definition 1. (Asaigeethan et al., 2024). A fuzzy set $\tilde{A} \subseteq X$ is introduced to represent imprecise or vague concepts that cannot be described using classical crisp sets. It is characterized by a collection of ordered pairs, where each element of the universal set X is associated with a membership value indicating its degree of belonging $\tilde{A} = \{(\eta, \mu_{\tilde{A}}(\eta)): f \in X, \mu_{\tilde{A}}(\eta) \in [0,1]\}$. Where $\mu_{\tilde{A}}(\eta)$ is a membership function (MF) of $\tilde{A}$, the mapping is measured as $\mu_{\tilde{A}}(\eta): X \longrightarrow [0,1]$.

Definition 2. (Asaigeethan et al., 2024). An $\alpha - cut$ of a fuzzy set $\tilde{A}$ is a crisp set $A_\alpha \subseteq X$ such that $A_\alpha = \{\eta / \mu_{\tilde{A}}(\eta) \geq \alpha\}$, $\alpha \in [0,1]$.

Definition 3. (Asaigeethan et al., 2024). A triangular fuzzy number (TFN) $\tilde{A} = (\xi_1, \xi_2, \xi_3)$ is defined by an associated membership function $\mu_{\tilde{A}}(\eta)$, which indicates each element of the membership function degree η with the specified interval, as given by

$$\mu_{\bar{A}}(\eta) = \begin{cases} \frac{\eta - \xi_1}{\xi_2 - \xi_1}, \text{for } \xi_1 \leq \eta \leq \xi_2 \\ \frac{\xi_3 - \eta}{\xi_3 - \xi_2}, \text{for } \xi_2 \leq \eta \leq \xi_3 \\ 0, \quad \text{elsewhere} \end{cases} \tag{1}$$

Using the α-cut method, a TFN with a maximum (at center), right width $\xi_3 - \xi_2 > 0$, and left width $\xi_2 - \xi_1 > 0$ is turned into interval numbers and written as $\tilde{A} = \{f_1', f_2']; [\theta_1, \theta_2]; [m_1, m_2]\} = [\xi_1 + (\xi_2 - \xi_1)\alpha, \epsilon_3 - (\xi_3 - \xi_2)\alpha]$, where $\alpha \in [0,1]$. **Figure 1** shows TFNs $\tilde{A} = (\xi_1, \xi_2, \xi_3)$ and the α-cut membership function. An arbitrary TFN meets the following conditions:

(i) f'_1, θ_1, m_1 and χ_1 are functions that get bigger on the interval [0, 1].
(ii) f'_2, θ_2, m_2 and χ_2 are functions that go down on the interval [0, 1].
(iii) $f'_1 \leq f'_2, \theta_1 \leq \theta_2, m_1 \leq m_2$ and $\chi_1 \leq \chi_2$ on the interval [0, 1].
(iv) $f'_1, f'_2, \theta_1, \theta_2, m_1, m_2, \chi_1, \chi_2$ are limited at [0, 1].

- $f'_1 = f'_2 = f'$, [f' is a crisp velocity].
- $\theta_1 = \theta_2 = \theta$, [$\theta$ is a crisp temperature].
- $m_1 = m_2 = m$, [m is a crisp concentration].

- $\chi_1 = \chi_2 = \chi$, [χ is a crisp microorganism].

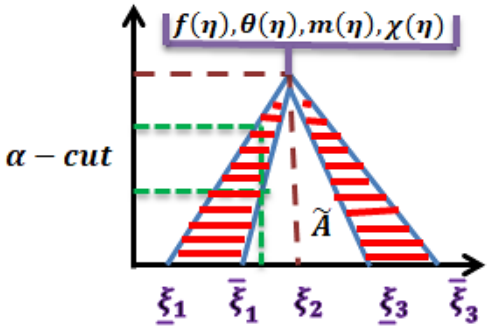

Figure 1. The MF of a TFN.

3. Mathematical Formulation

Consider a steady, 2D, incompressible nanofluid flow over a heated stretching sheet positioned at $y = 0$ as shown in **Figure 2**. The surface stretches in the x-direction with a linear velocity $U_w = ax$, while the ambient fluid moves with a free-stream velocity $U_\infty(x) = bx$, corresponding to a stagnation-point flow arrangement. A uniform magnetic field of strength B_0 is applied perpendicular to the flow field. The assumption of a low magnetic Reynolds number $Re \ll 1$ for liquid nanofluid flow leads to greater magnetic diffusion than induction, resulting in the neglect of the induced magnetic field. In contrast to plasma regimes, weakly ionized, water-based nanofluids with high electron–collision frequency have negligible Hall and ion-slip effects. Furthermore, the influence of any external electric field is ignored, and the electric field arising from charge polarization effects is assumed to be insignificant. Under these conditions, the governing steady boundary layer equations for 2D Sutterby hybrid nanofluid flow are formulated, accounting for simplified H-H chemical reactions.

$$\wp + 2\mathbb{Q} \rightarrow 3\mathbb{Q}, \qquad \text{rate} = d_c p q^2 \tag{2}$$

A first-order isothermal chemical reaction is assumed to occur at the catalyst surface.

$$\wp \rightarrow \mathbb{Q}, \qquad \text{rate} = d_s p \tag{3}$$

$$u\partial_x u + v\partial_y u = 0 \tag{4}$$

$$u\partial_x u + v\partial_y u = \nu_{hnf}\left[\partial_{yy}u + \frac{nE^2}{2}\left(\partial_y u\right)^2 \partial_{yy}u\right] - \frac{\sigma_{hnf}B_0^2}{\rho_{hnf}}(u - u_\infty) \tag{5}$$

$$u\partial_x T + v\partial_y T = \alpha_{hnf}\partial_{yy}T + \frac{\nu_{hnf}}{C_{hnf}}\left(\partial_y u\right)^2 - \frac{1}{(\rho c)_{hnf}}\partial_y(q_r) + \frac{\sigma_{hnf}B_0^2}{(\rho c)_{hnf}}(u_\infty - u)^2 + \tau\left[D_B\partial_y p\partial_y T + \frac{D_T}{T_\infty}\left(\partial_y T\right)^2\right] \tag{6}$$

$$u\partial_x p + v\partial_y p = D_\wp\partial_{yy}p + \frac{D_T}{T_\infty}\partial_{yy}T - d_c p q^2 \tag{7}$$

$$u\partial_x q + v\partial_y q = D_\mathbb{Q}\partial_{yy}q + \frac{D_T}{T_\infty}\partial_{yy}T + d_s p q^2 \tag{8}$$

$$u\partial_x N + v\partial_y N = D_N\left(\partial_{yy}N\right) - \frac{b^* W_c}{(C_W - C_\infty)}\partial_y\left[N\partial_y p\right] \tag{9}$$

$$u = U_w(x) = ax + l_1\partial_y u, v = 0, T = T_w + l_2\partial_y T, D_\wp\left(p_w + l_3\partial_y p\right) = l_s p, D_\mathbb{Q}\left(q_w + l_3\partial_y q\right) = -l_s q, N = N_w + l_4\partial_y N \text{ at } y \rightarrow 0, u = U_\infty(x) = bx, T \rightarrow T_\infty, p \rightarrow p_\infty, q \rightarrow q_\infty, N \rightarrow N_\infty \text{ at } y \rightarrow \infty \tag{10}$$

Table 1. Physicochemical attributes of the nanoparticles.

Thermal properties	$\sigma(\Omega^{-1}\,cm^{-1})$	$\kappa(Wm^{-1}K^{-1})$	$\rho\ (kgm^{-3})$	$C_p(Jkg^{-1}K^{-1})$
$CdSe$	1.4×10^{7}	0.45	5.82	258
$(C_6H_{11}NO_4)_n$	1.91×10^{-6}	0.5	1000	910
$Blood$	0.006	$0.49-0.55$	1060	3.21×10^{3}

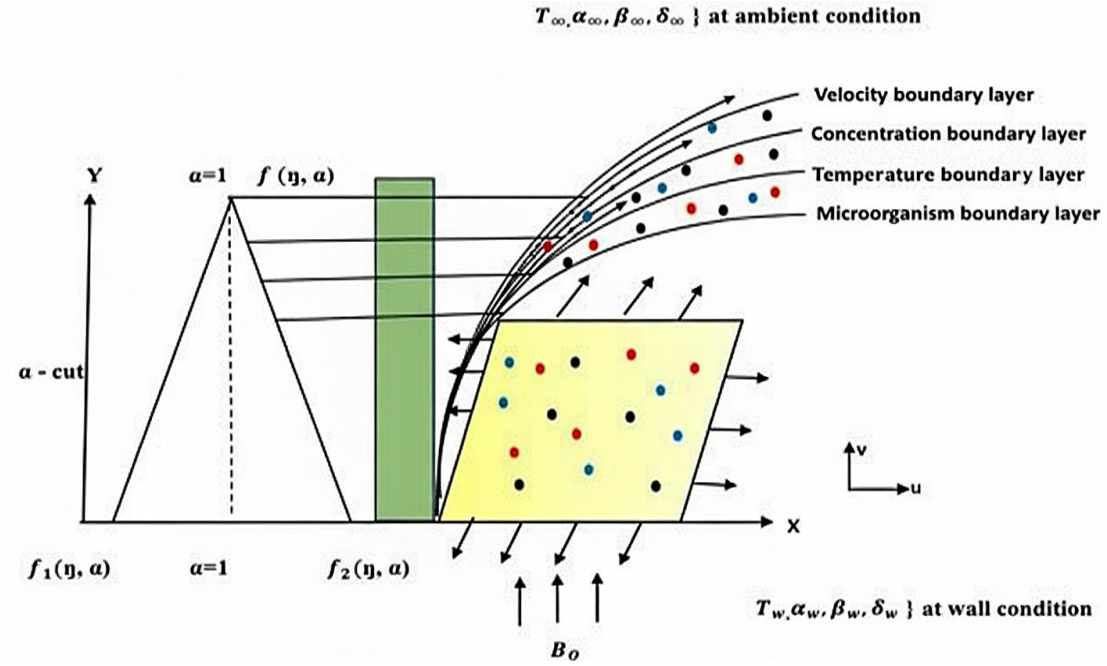

Figure 2. Thermal flow physical model.

Let p and q denote the concentrations of the hybrid nanoparticles. The stretching surface is assumed to move with a linear velocity $U_w(x) = ax$, where $a > 0$ represents the stretching rate and x is the spatial coordinate measured along the surface. To model thermal radiation effects, the Rosseland diffusion approximation is employed under the assumption of an optically thick medium. Accordingly, the radiative heat flux is provided by Shaw et al. (2022) and Patil and Goudar (2023),

$$q_r = -\frac{4\sigma^*}{3k^*}\partial_y T^4 = -\frac{16\sigma^*}{3k^*}\,T^3\partial_y T \tag{11}$$

Here, σ^* denotes the Stefan–Boltzmann constant, and k^* represents the mean absorption coefficient of the medium. Introducing the following transformation to convert governing equations into dimensionless form,

$$\eta = \sqrt{\frac{a}{\upsilon_f}}y,\ u = axf'(\eta), v = -\sqrt{a\upsilon_f}f(\eta),\quad \theta(\eta) = \frac{T-T_\infty}{T_w-T_\infty}\quad \text{With } T = T_\infty(1+(\theta_w-1)\theta),\quad N(\eta) = \frac{N-N_\infty}{N_w-N_\infty} \text{ and } m(\eta) = \frac{p-q_\infty}{p_w-p_\infty}, n(\eta) = \frac{q-q_\infty}{q_w-q_\infty} \tag{12}$$

The right-hand side of the Equations (6) and (11) given,

$$u\partial_x T + v\partial_y T = \partial_y T\left[\left(\alpha_{hnf} + \frac{16\sigma^* T^3}{3(\rho c)_{hnf}\, k^*}\right)\partial_y T\right]\ \partial_{yy} T + \frac{\nu_{hnf}}{C_{hnf}}\left(\partial_y u\right)^2 - \frac{1}{(\rho c)_{hnf}}\partial_y (q_r) + \frac{\sigma_{hnf} B_0^2}{(\rho c)_{hnf}}(u_\infty - u)^2 + \tau\left[D_B \partial_y p.\, \partial_y T + \frac{D_T}{T_\infty}\left(\partial_y T\right)^2\right] \quad (13)$$

Rewrite the first term on the right side of the Equation (13) as
$\alpha_{hnf}\ \partial_y\left[\partial_y T(1 + R_d(1 + (\theta_w - 1)\theta^3)\right]$,

where, R_d is the radiation parameter and it is denoted by $\frac{16\sigma^* T_\infty^3}{3kk^*}$, if $R_d = 0$ gives no thermal radiation effect.

After applying the described transformation Equation (12), the governing Equations (5), (7), (8), (9), and (13) take the following form:

$$\frac{f'''(\eta)}{D_1 D_2}\left[1 + \frac{n}{2} D_e Re_x (f''(\eta)\,)^2\ \right] - (f'(\eta)\,)^2 + f(\eta)\, f''(\eta)\ + \frac{D_4 D_5}{D_2} B\left(\lambda - f'(\eta)\right) = 0 \quad (14)$$

$$\frac{1}{Pr}[(1 + R_d(1 + (\theta_w - 1)\theta^3)\ \theta'(\eta)]' + f(\eta)\theta'(\eta) + \frac{1}{D_1 D_2} Ec\left(f''(\eta)\right)^2 + \frac{D_4 D_5}{D_3} BEc(\lambda - f'(\eta)\,)^2 + Nbm(\eta)'\theta(\eta)' + Nt(\theta'(\eta))^2 = 0 \quad (15)$$

$$\frac{1}{Sc}\left[m''(\eta) + \frac{N_t}{N_b}\theta''(\eta)\right] + f(\eta)\, m'(\eta) - Lm(\eta) n(\eta)^2 = 0 \quad (16)$$

$$\frac{\delta}{Sc}\left[n''(\eta) + \frac{N_t}{N_b}\theta''(\eta)\right] + f(\eta)\, n'(\eta) + Lm(\eta) n(\eta)^2 = 0 \quad (17)$$

$$\chi''(\eta) - Pe[m''(\eta)(\chi(\eta) + \omega) + m'(\eta)\chi'(\eta)] + Lbf(\eta)\, \chi'(\eta) = 0 \quad (18)$$

Corresponding boundary conditions are

$$f(0) = 0,\ f'(0) = 1 + c_1 f''(0), \theta(0) = 1 + c_2\theta'(0),\ Lsm'(0) = 1 + c_3 m(0),\ \delta Lsn'(0) = -(1 + c_3 n(0)),\ \chi(0) = 1 + c_4\chi'(0), f'(\infty) = \lambda, \theta(\infty) = 0, m(\infty) = 1, n(\infty) = 1, \chi(\infty) = 0 \quad (19)$$

Let's say that the diffusion coefficients for both substances $D_{\wp}$ and $D_{\mathbb{Q}}$ are the same ($i.e., \alpha = 1$), Then,

$$m(\eta) + n(\eta) = 1 \quad (20)$$

The concentration Equations (16) & (17) convert to the form by the above transformation

$$\frac{1}{Sc}\left[m''(\eta) + \frac{N_t}{N_b}\theta''(\eta)\right] + f(\eta)\, m'(\eta) - Lm(\eta) - (1 - m(\eta))^2 = 0 \quad (21)$$

Subject to the boundary condition,

$$m'(0) = Ls\, m(0),\ m(\infty) = 1 \quad (22)$$

The physical parameters used for this study are relevant to actual engineering and industrial applications. The Deborah number indicates viscoelastic behavior in biological and polymeric fluids, whereas the magnetic field simulates MHD flow control utilized in cooling channels and pumps. Catalytic systems and solar-thermal processes both depend on radiation and chemical reaction parameters. In surface-engineered channels and microfluidics, slip effects occur, and in bioreactors, bioconvective characteristics reflect mixing caused by microorganisms. Realistic uncertainty in the manufacturing of nanofluids is

captured by fuzzy nanoparticle volume fractions. These factors support the choice of parameters employed in this investigation.

Table 2. Non-dimensional physical parameters.

D_e		$\frac{E^2a^2}{\upsilon_f}$
Re		$\frac{a^2x}{\upsilon_f}$
B		$\frac{\sigma_f B_0^2}{\rho_f a}$
λ		$\frac{p}{l}$
Pr		$\frac{\nu_f}{\alpha}$
Ec		$\frac{U_w^2}{C_f}$
Sc		$\frac{\nu_f}{D_A}$
δ		$\frac{D_B}{D_A}$
N_b		$\frac{\tau D_B(e_w - e_\infty)}{\sigma_f}$
N_t		$\frac{\tau D_T(T_w - T_\infty)}{T_\infty \sigma_f}$
Pe		$\frac{b^* W_c}{D_m}$
Lb		$\frac{\upsilon_f}{D_m}$
ω		$\frac{M_\infty}{M_w - M_\infty}$
Viscosity	D_1	$[(1-\varphi_1)^{2.5}(1-\varphi_2)^{2.5}]$
Density	D_2	$(1-\varphi_2)\left[1-\varphi_1+\varphi_1\frac{\rho_{s1}}{\rho_f}\right]+\varphi_2\frac{\rho_{s2}}{\rho_f}$
Electrical conductivity	D_3	$\left(\frac{\sigma_2+2\sigma_{nf}-2\varphi_2(\sigma_{nf}-\sigma_2)}{\sigma_2+2\sigma_{nf}+\varphi_2(\sigma_{nf}-\sigma_2)}\right)$
Thermal conductivity	D_4	$(1-\varphi_2)\left[1-\varphi_1+\varphi_1\frac{(\rho C_p)_{s1}}{(\rho C_p)_f}\right]+\varphi_2\frac{(\rho C_p)_{s2}}{(\rho C_p)_f}$
Heat Capacity	D_5	$\frac{k_{s2}+2k_{nf}+2\varphi_2(k_{s2}-k_f)}{k_{s2}+2k_{nf}-2\varphi_2(k_{s2}-k_f)}$

4. Method of Solution

The MATLAB solver bvp5c is used to numerically solve the system of coupled ordinary differential equations (ODEs) given by Equations (14), (15), (18), and (21), with the boundary conditions in Equations (19) and (22). Because it uses an adaptive mesh strategy and has reliable convergence properties, this routine is excellent for solving very nonlinear boundary-value problems. The continuous solution's residual control makes it possible to improve the mesh and control errors. So, the governing equations are changed into a first-order system that is the same, and Equations (14), (15), (18), and (21) are rewritten like this:

$$f = k_1, f' = k_2, f'' = k_3, f''' = k_3', \theta = k_4, \theta' = k_5, \theta'' = k_5', m = k_6, m' = k_7, m'' = k_7', \chi = k_8, \chi' = k_9, \chi'' = k_9' \quad (23)$$

$$\mathcal{H}_1 = k_3' = \frac{D_1 D_2\left[k_2^2 - k_1 k_3 - \frac{D_4 D_5}{D_2} B(\lambda - k_2)\right]}{1+\frac{n}{2} De Re (k_3)^2} \tag{24}$$

$$\mathcal{H}_2 = k_5' = \frac{-\left[k_1 k_5 + \frac{1}{D_3 D_4} Ec k_3^2 + \frac{D_1 D_2}{D_5} BEc(\lambda - k_2)^2 + Nb k_7 k_5 + Nt(k_5)^2\right]}{\frac{1}{Pr}\left(1+R_d\left(1+(\theta_w - 1){k_4}^3\right)\right.} \tag{25}$$

$$\mathcal{H}_3 = k_7' = \frac{-\left[k_7 k_1 + \frac{1}{Sc}\frac{N_t}{N_b}\mathcal{H}_2\right] + Lk_6(1-k_6)^2}{\frac{1}{Sc}} \tag{26}$$

$$\mathcal{H}_4 = k_9' = Pe[\mathcal{H}_3(k_8 + \omega) + k_7 k_9] - Lbk_1 k_9 \tag{27}$$

With boundary conditions:

$$k_1 = 0, k_2 = 1 + c_1 k_3, k_4 = 1 + c_2 k_5,\ Lsk_7 = 1 + c_3 k_6,\ k_8 = 1 + c_4 k_9, at\ \eta = 0, k_2 = \lambda, k_4 = 0, k_6 = 1, k_8 = 0\ at\ \eta = \infty \tag{28}$$

Prior to using the boundary value problem method (bvp5c) to solve a set of first-order ODEs, we chose detrimental initial estimates for $k_3(0), k_5(0), k_7(0)$ and $k_9(0)$ as -1, 1, 1, and 1, respectively. So, until the required convergence conditions are met, if the accepted error is less than the perimeter residuals of $\mathcal{H}_1, \mathcal{H}_2, \mathcal{H}_3$ and $\mathcal{H}_4$, then the process will continue.

5. Physical Estimations

$$Cf_x = \frac{2\tau_w}{\rho u_w^2}, Nu_x = \frac{x q_w}{k(T_f - T_\infty)}, Sh_x = \frac{x m_w}{D_B(C_w - C_\infty)}, Nh_x = \frac{x n_w}{D_m(N_w - N_\infty)} \tag{29}$$

The expressions for wall shear stress, heat transfer rate, mass transfer rate, and motile microorganism density are defined as

$$\tau_w = -\mu_0\left[\partial_y u + \frac{nE^2}{6}\left(\partial_y u\right)^3\right]_{y=0}, q_w = -k\left(\partial_y T\right), m_w = -k\left(\partial_y m\right), n_w = -k\left(\partial_y N\right) \tag{30}$$

The corresponding dimensionless representations of the above physical quantities are given by

$$\sqrt{Re_x} Cf_x = \left[f''(0) + \frac{1}{6} nDe\, Re_x\left(f''(0)\right)^3\right] \tag{31}$$

$$\frac{1}{\sqrt{Re_x}} Nu_x = -\left(1 + \frac{4}{3}Rd\right)\theta'(0) \tag{32}$$

$$\frac{1}{\sqrt{Re_x}} Sh_x = -\phi'(0) \tag{33}$$

$$\frac{1}{\sqrt{Re_x}} Nh_x = -\chi'(0) \tag{34}$$

where, $Re_x = \frac{ax^2}{\upsilon_f}$ is the local Reynolds number.

6. Fuzzification Scheme

In addition, this study investigates a comparative analysis of bi-nanofluids using fuzzy logic concepts. The volume proportion of the hybrid nanofluid is represented as a TFN, which leads to the transformation of the governing nonlinear ordinary differential equations (ODEs) into fuzzy differential equations (FDEs). The resulting FDEs are solved numerically using the MATLAB solver bvp5c. Variations in the volume fraction of the hybrid nanofluid have a direct influence on both the heat transverse characteristics and the fluid velocity, which are the primary factors governing the thermal performance and flow

behavior of the hybrid nanofluid. Previous studies report that the nanoparticle volume proportion typically lies within the range [0.01-0.04]. Since φ_1 and φ_2 denote the volume fractions of the nanoparticles $CdSe$ and $(C_6H_{11}NO_4)_n$ respectively, a fuzzy modeling framework is adopted to address uncertainty by expressing these parameters as TFNs. The thermophysical properties of the nanoparticles are listed in **Table 2**. The TFNs corresponding to the nanoparticle volume fractions are further converted into α-cut representations, which regulate the degree of fuzziness.

Table 3 also presents the TFNs alongside their associated crisp values. The membership values of the fuzzy numbers are evaluated over the interval $\alpha \in [0,1]$, defining the triangular membership functions. Using the α-cut technique, the nonlinear ODEs (14), (15), (18), and (21), along with their respective boundary conditions, are transformed into FDEs and solved to obtain the fuzzy solutions.

$$\frac{1}{D_1 D_2}\partial_{\eta\eta\eta}[f_1,f_2]\left[1+\frac{n}{2}D_e Re_x\left(\partial_{\eta\eta}[f_1,f_2]\right)^2\right]-\left(\partial_{\eta}[f_1,f_2]\right)^2+[f_1,f_2].\partial_{\eta\eta}[f_1,f_2]+\frac{D_4D_5}{D_2}B\left(\lambda-\partial_{\eta}[f_1,f_2]\right)=0 \quad (35)$$

$$\frac{1}{Pr}\left[(1+R_d(1+(\theta_w-1)\theta^3)\,\partial_{\eta}[\theta_1,\theta_2]\right]'+[f_1,f_2].\partial_{\eta}[\theta_1,\theta_2]+\frac{1}{D_1 D}Ec\left(\partial_{\eta\eta}[f_1,f_2]\right)^2+\frac{D_4D_5}{D_3}BEc\left(\lambda-\partial_{\eta}[f_1,f_2]\right)^2+Nb\partial_{\eta}[m_1,m_2].\partial_{\eta}[\theta_1,\theta_2]+Nt\left(\partial_{\eta}[\theta_1,\theta_2]\right)^2=0 \quad (36)$$

$$\frac{1}{Sc}\left[\partial_{\eta\eta}[m_1,m_2]+\frac{N_t}{N_b}\partial_{\eta\eta}[\theta_1,\theta_2]\right]+[f_1,f_2]\partial_{\eta}[m_1,m_2]-L[m_1,m_2](1-[m_1,m_2])^2=0 \quad (37)$$

$$\partial_{\eta\eta}[\chi_1,\chi_2]-Pe\left[[\chi_1,\chi_2].\partial_{\eta\eta}[m_1,m_2]+\partial_{\eta}[\chi_1,\chi_2].\partial_{\eta}[m_1,m_2]\right]+Lb[f_1,f_2]\,\partial_{\eta}[\chi_1,\chi_2]=0 \quad (38)$$

The consistent boundary conditions are

$$[f_1(0,\alpha),f_2(0,\alpha)]=0,\partial_{\eta}[f_1(0,\alpha),f_2(0,\alpha)]=1+c_1\partial_{\eta\eta}[f_1(0,\alpha),f_2(0,\alpha)],[\theta_1(0,\alpha),\theta_2(0,\alpha)]=1+c_2\partial_{\eta}[\theta_1(0,\alpha),\theta_2(0,\alpha)],Ls\;\partial_{\eta}[m_1(0,\alpha),m_2(0,\alpha)]=1+c_3[m_1(0,\alpha),m_2(0,\alpha)],[m_1(\infty,\alpha),m_2(\infty,\alpha)]=1\,,[\chi_1(0,\alpha),\chi_2(0,\alpha)]=1+c_4\partial_{\eta}[\chi_1(0,\alpha),\chi_2(0,\alpha)],\partial_{\eta}[f_1(\infty,\alpha),f_2(\infty,\alpha)]=\lambda,[\theta_1(\infty,\alpha),\theta_2(\infty,\alpha)]=0 \quad (39)$$

Table 3. Volume fraction of TFNs of nanoparticles.

Crisp Value for nanoparticles		TFN	α − cut approach
$\varphi_1(CdSe)$	0.04	$[0, 0.05, 0.1]$	$[0.05\alpha, 1-0.05\alpha], \alpha \in [0\ ,1]$
$\varphi_2(C_6H_{11}NO_4)_n$	0.04	$[0, 0.05, 0.1]$	$[0.05\alpha, 1-0.05\alpha], \alpha \in [0\ ,1]$

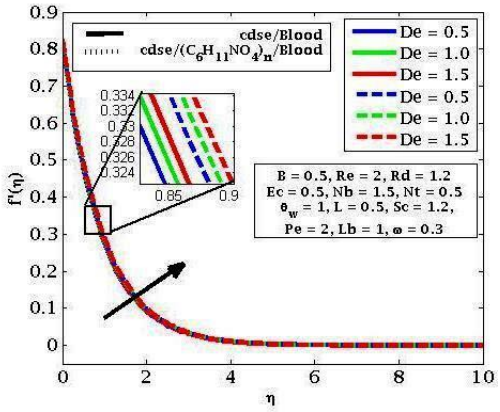

Figure 3. Velocity effect on De.

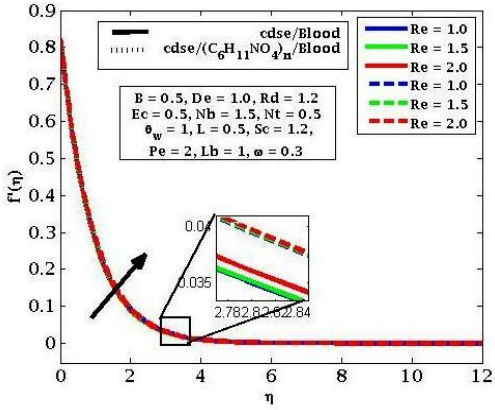

Figure 4. Velocity effect on Re.

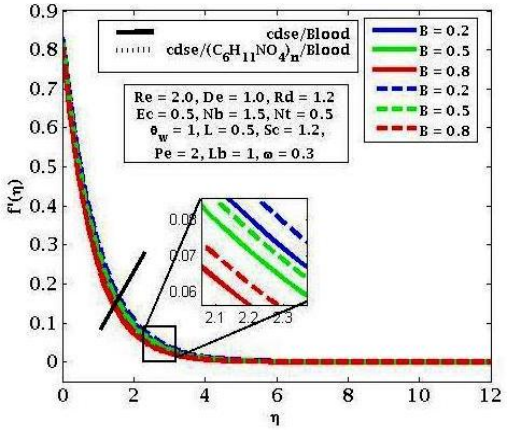

Figure 5. Velocity effect on B.

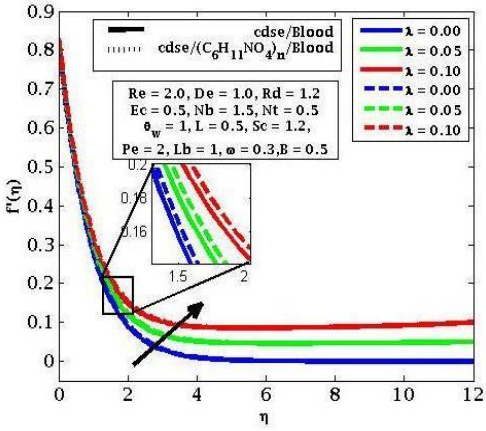

Figure 6. Velocity effect on λ.

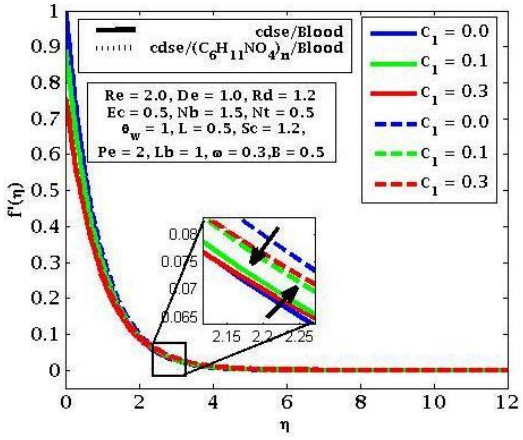

Figure 7. Velocity effect on c_1.

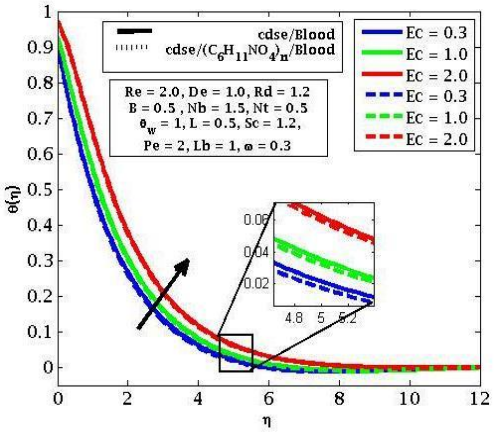

Figure 8. Temperature effect on Ec.

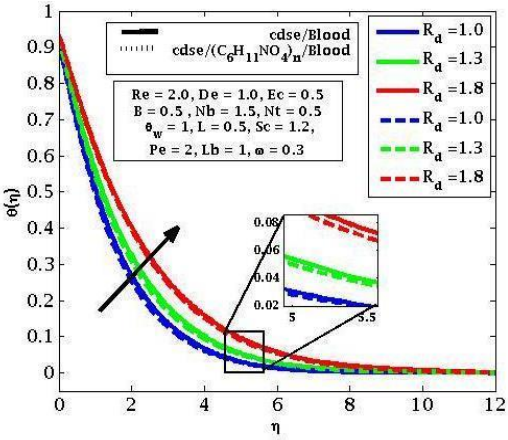

Figure 9. Temperature effect on R_d.

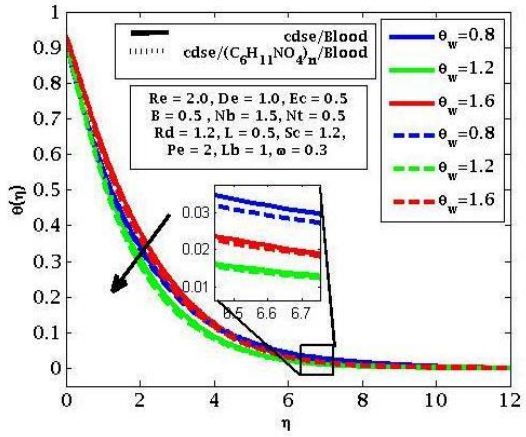

Figure 10. Temperature effect on θ_w.

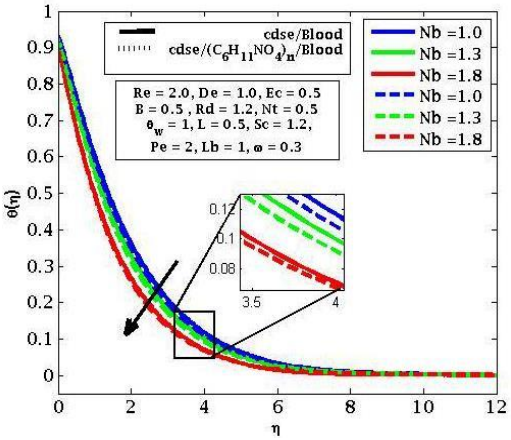

Figure 11. Temperature effect on Nb.

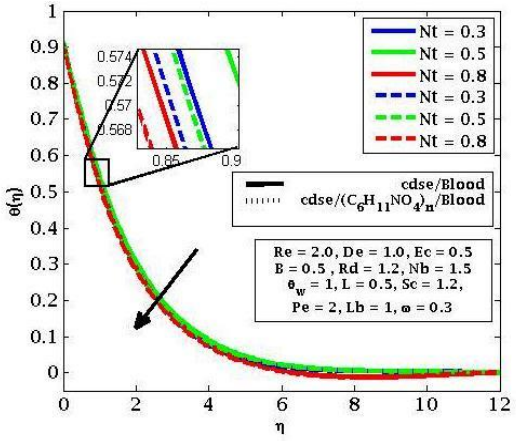

Figure 12. Temperature effect on Nt.

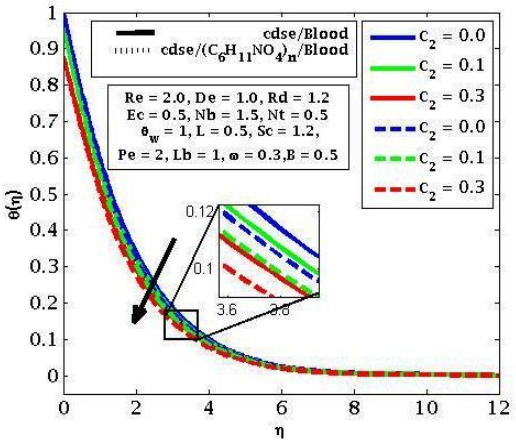

Figure 13. Temperature effect on c_2.

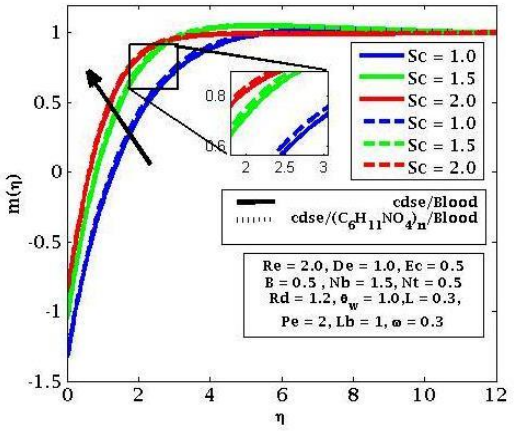

Figure 14. Concentration effect on Sc.

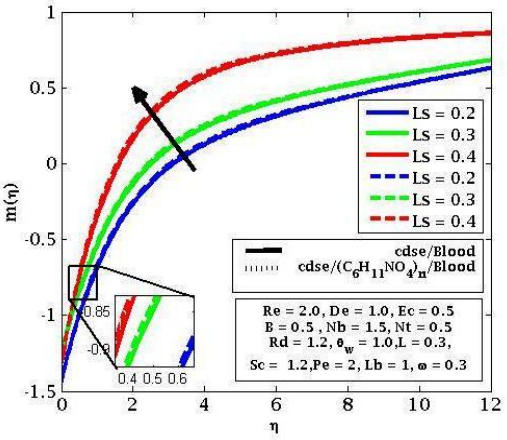

Figure 15. Concentration effect on Ls.

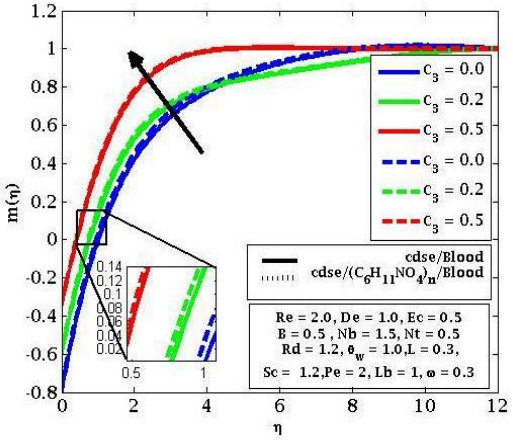

Figure 16. Concentration effect on c_3.

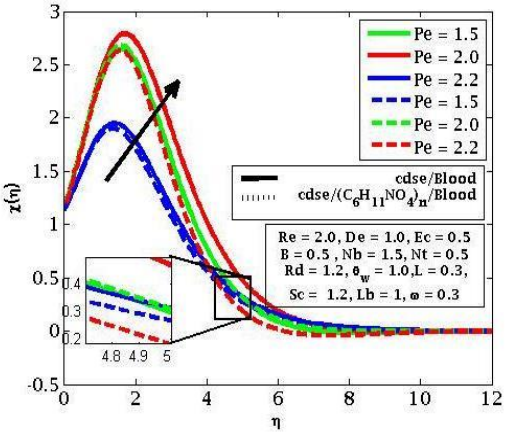

Figure 17. Microorganism effect on Pe.

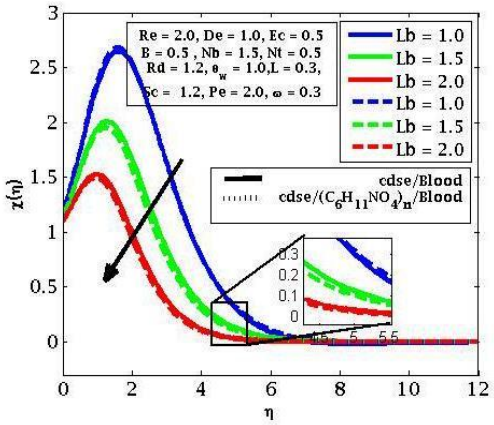

Figure 18. Microorganism effect on Lb.

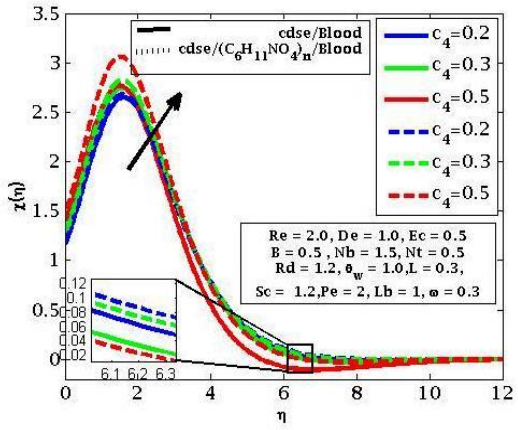

Figure 19. Microorganism effect on c_4 .

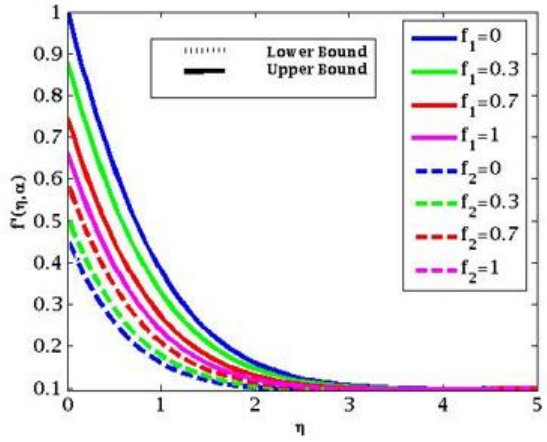

Figure 20. Fuzzy velocity.

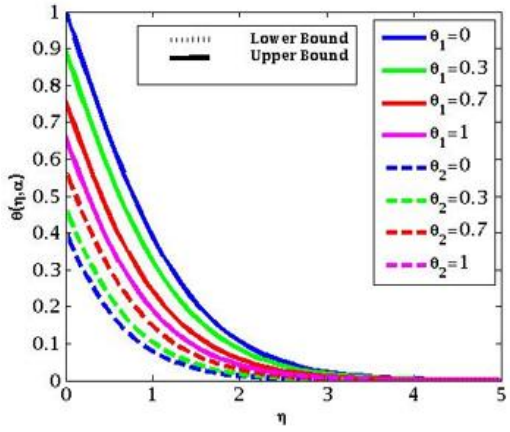

Figure 21. Fuzzy temperature.

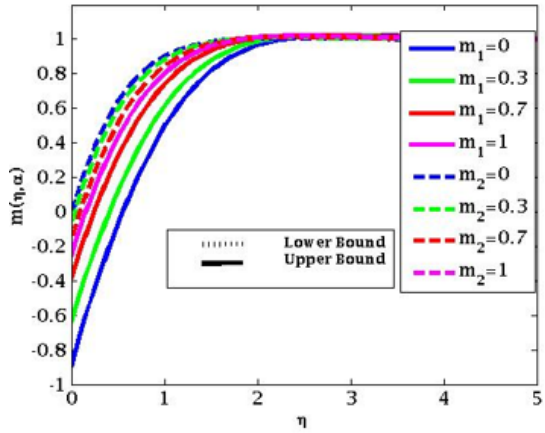

Figure 22. Fuzzy concentration.

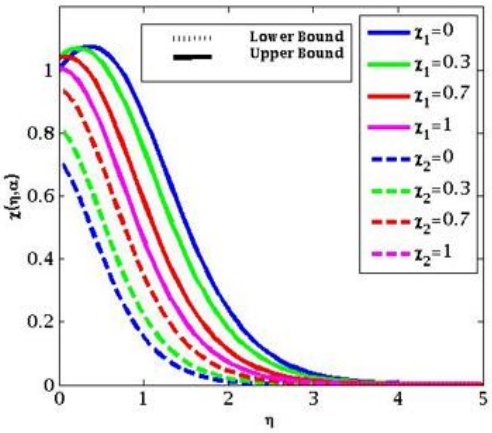

Figure 23. Fuzzy microorganism.

7. Results and Discussion

7.1 Velocity Profile

Figures (3-7) illustrate the substantial impacts of the Deborah number (De), Reynolds number (Re), magnetic field parameter (B), velocity ratio (λ), and velocity slip parameter (c_1) on the fluid velocity profiles of nanofluid and hybrid nanofluid. The influences are analyzed in the context of constant power law index number $n = 0.4$ flow characteristics. **Figure 3** demonstrates that, within the divergent flow regime, an elevation in the Deborah number (De) amplifies the elastic characteristics of both nanofluids and hybrid nanofluids as a result of extended retardation effects. The improved elasticity decreases the effective viscosity of the fluid, therefore increasing the flow velocity. As a result, elevated velocities are noted for nanofluids and hybrid nanofluids, enhancing convective heat transfer from the stretching surface. **Figure 4** indicates that a higher Reynolds number (Re) enhances the fluid velocity profile by promoting the dominance of inertial forces over viscous resistance, as a higher Re allows fluid to move more efficiently for $n = 0.4$. In **Figure 5**, as the magnetic field (B) increases, the velocity of the fluid decreases because the Lorentz force suppresses electrical conductivity. As a result of magnetic permeability, the velocity distribution in the hybrid nanofluid is stronger than that in the nanofluid. This phenomenon occurs at $n = 0.4$. **Figure 6** when the velocity ratio (λ) increases in the direction of flow, it leads to a flatter velocity profile by reducing the thickness of the momentum boundary layer, which in turn causes the velocity to increase at $n = 0.4$. **Figure 7** depicts the enhanced velocity slip parameter (c_1) at $n = 0.4$ the fluid, which increases the velocity profile of the nanofluid because the near-wall velocity is reduced, which effectively pushes the boundary layer further out and makes it thicker; however, the velocity profile of the hybrid nanofluid decreases due to its proximity to the surface.

7.2 Temperature Profile

Figures (8-13) depict the effects of the Eckert number (Ec), radiation parameter (R_d), temperature ratio parameter (θ_w), Brownian motion parameter (Nb), thermophoresis parameter (Nt), and thermal slip boundary parameter (c_2) on the temperature profiles of Sutterby nanofluids and hybrid nanofluids. The analysis is carried out using the constant power law index at $n = 0.4$ of the flow regimes. **Figure 8** indicates that increasing the Eckert number (Ec) elevates the temperature profiles of both nanofluids and hybrid nanofluids due to enhanced viscous dissipation, which thickens the thermal boundary layer. In **Figure 9**, increasing the radiation parameter (R_d) thickens the thermal boundary layer, improving the temperature profile. Nanoparticles make nanofluids and hybrid nanofluids better at absorbing and scattering thermal energy. Higher R_d values increase radiative heat transfer, raising surface temperature and expanding the thermal boundary layer, which is critical to heat dissipation. **Figure 10** shows that increasing the temperature ratio parameter (θ_w) increases the thermal field by increasing temperature distribution and thickening the thermal boundary layer. Enhanced thermophoretic transport and Brownian motion improve heat transmission but increase thermal radiation near the stretching surface. Higher θ_w values improve temperature regulation in hybrid nanofluids by redistributing thermal energy and stabilizing the thermal profile. **Figure 11** depicts Brownian motion (Nb), caused by temperature differences, promoting random nanoparticle movement in fluids and improving heat transmission. A higher Nb enhances thermal energy dispersion and improves the temperature profile in nanofluids containing only one type of nanoparticle. As the thermal boundary layer thickens, thermal radiation or magnetic field effects reduce the temperature gradient, limiting nanoparticle mobility and Brownian diffusion. Thus, smaller Nb values reduce heat transfer. Synergistic interactions initially accelerate Brownian motion in hybrid nanofluids, but boundary-layer growth reduces the temperature gradient, which reduces heat transfer performance. **Figure 12** demonstrates that rising Nt increases fluid temperature difference and nanoparticle thermophoretic force. Nanoparticles bring thermal energy from hot to cold, raising fluid temperature. Higher nanoparticle concentrations raise nanofluid and hybrid

nanofluid temperatures, enhancing this process. Proper Nt adjustment improves thermal regulation, extended surface heat dissipation, and thermal radiation effects by controlling the temperature gradient and thermophoretic transport. **Figure 13** indicates how the thermal slip parameter (c_2) affects temperature distribution. Increased c_2 results in lower fluid temperature near the surface due to reduced thermal interaction with the boundary. Thermal slip relaxes the thermal boundary condition, allowing fluid surface interaction and more effective heat evacuation from solid surfaces. Therefore, a larger thermal slip lowers the temperature profile by increasing heat loss from the border.

7.3 Concentration Profile

Figures (14-16) demonstrate how the Schmidt number (Sc), the H-H reaction parameter (Ls), and the concentration slip parameter (c_3) affect the concentration profiles of nanofluids and hybrid nanofluids. The analysis is conducted using the constant power law index number at $n = 0.4$ for the flow characteristics. **Figure 14** shows that increasing the Schmidt number (Sc) decreases mass diffusivity, lowering fluid concentration and steepening the concentration gradient. Higher Sc values inhibit species diffusion in nanofluids and hybrid nanofluids, accelerating concentration decline. With increasing Sc, mass diffusivity diminishes, limiting nanoparticle and solute species dispersion and mass and heat transmission. Thus, Schmidt number control can regulate concentration gradients and optimize mass transfer in hybrid nanofluids, improving thermal management around the stretching surface. **Figure 15** indicates how the homogeneous-heterogeneous reaction parameter (Ls) affects nanofluid and hybrid concentration distribution. In homogeneous reaction-dominated flows, increasing the reaction rate thickens the concentration boundary layer and raises its concentration. Due to species consumption on the surface, heterogeneous reactions with higher reaction rates lower the concentration profile. In hybrid nanofluids, heterogeneous reactions increase the concentration gradient, whereas homogeneous reactions decrease it. Controlling the concentration field by tweaking homogeneous and heterogeneous reaction rates optimizes mass transfer and thermal regulation of the flow system. **Figure 16** demonstrates that the concentrations slip parameter (c_3) significantly affects the concentration distribution of nanofluids and hybrid nanofluids. Increasing c_3 weakens particle-fluid interaction in the concentration boundary layer, reducing fluid concentration near the border. Adjusting the concentration slip parameter effectively controls species concentration, improving heat and mass transport and reducing thermal radiation.

7.4 Microorganism Profile

Figure 17 indicates that the Peclet number (Pe) strongly affects gyrotactic microbe dispersion in nanofluids and hybrid nanofluids. Peclet number enhances motile microbe concentration, expanding the bioconvective boundary layer. Because advective transport dominates diffusive transport, microbes aggregate in specific flow areas. Nanofluids have a weak effect, but hybrid nanofluids have better thermal and mass transport capabilities, creating a thicker motile microbe boundary layer. **Figure 18** illustrates that when the bioconvection Lewis number (Lb) increases, motile microbe concentration drops in nanofluids and hybrid nanofluids. Lower mass diffusivity limits microorganism transport and dispersion in fluids. Multiple nanoparticles in hybrid nanofluids interact complexly with motile bacteria, causing a greater concentration drop. Hybrid nanofluids with optimized Lewis numbers can control microbe dispersal, making bioconvective flow more stable. **Figure 19** depicts how the microorganism slip boundary parameter (c_4) affects the distribution and flow properties of motile microorganisms in nanofluids and hybrid nanofluids. Microorganisms change drag forces, especially in slip situations, by modifying the velocity field. Increased microbe slip reduces hydrodynamic resistance and allows a non-zero boundary velocity, which influences transport and flow mobility.

7.5 Fuzzification Profile

The fuzzy modeling framework adopted for the governing parameters facilitates the development of a more precise and patient-specific drug delivery design by identifying an optimal dosage that is both functionally effective and economically viable. **Figure 20** illustrates the influence of the fuzzy volume fraction on the velocity distribution of the Sutterby hybrid nanofluid. The velocity profile $f'(\eta,\alpha)$is bounded by the upper and lower solutions $f'_1(\eta,\alpha)$ and $f'_2(\eta,\alpha)$ respectively. The α-cut levels considered in the analysis are $\alpha = 0, 0.3, 0.7$, and 1. Within this interval, an optimal solution region is observed, and the velocity profiles converge as the α approaches unity, resulting in coinciding curves. **Figure 21** depicts how the fuzzy volume proportion affects the temperature flow of the Sutterby hybrid nanofluid. The temperature profile $\theta(\eta,\alpha)$ is contained by the lower bound $\theta_1(\eta,\alpha)$ and upper bound $\theta_2(\eta,\alpha)$. The application of the fuzzy framework within the prescribed α-cut range yields an optimized thermal response, with the temperature profiles merging at $\alpha = 1$. The impact of the fuzzy volume fraction on the concentration profile is depicted in **Figure 22**. Here, $m(\eta,\alpha)$ represents the concentration variation bounded by the upper and lower limits $m_1(\eta,\alpha)$ and $m_2(\eta,\alpha)$.The selected α-cut values 0,0.3,0.7 and 1 are examined to identify the optimal concentration behavior, with complete convergence of the profiles occurring at $\alpha = 1$. **Figure 23** demonstrates the influence of the fuzzy volume proportion on the microorganism concentration profile of the Sutterby hybrid nanofluid. The microorganism density $\chi(\eta,\alpha)$ varies within the bounds defined by $\chi_1(\eta,\alpha)$ and $\chi_2(\eta,\alpha)$. An optimal response is achieved within the considered α-cut range, and the profiles coincide at $\alpha = 1$ indicating the elimination of uncertainty.

8. Validation of Result

In an extreme case where hybrid nanoparticle affects, non-Newtonian parameters, chemical reactions, slip, and bioconvection are disregarded, the current model simplifies to the formulation proposed by Mushtaq et al. (2014) as shown in **Table 4**. The diminished Nusselt number acquired in this limit aligns quite well with the published findings, thus verifying the numerical methodology.

Table 4. The reduced local Nusselt value$-\theta'(0)$ at $\varphi_1 = \varphi_2 = 0, B = 0.5, Pr = 7, \lambda = 0.5, R_d = 1, Ec = 0.2, \theta_w = 1.5, Sc = 10, Ls = 0.5, Lb = 2$, and $Pe = 1$.

Nb	Nt					
	0.1		0.3		0.5	
	Mushtaq et al. (2014)	Present value	Mushtaq et al. (2014)	Present value	Mushtaq et al. (2014)	Present value
0.1	0.081387	0.098221	0.080637	0.098168	0.079801	0.088115
0.3	0.074496	0.088193	0.073172	0.088135	0.071680	0.088076
0.5	0.065911	0.078170	0.063892	0.078106	0.061644	0.078042

Table 5 shows how the velocity ratio (λ), Deborah number (De), Reynolds number (Re), magnetic field parameter (B), and α-cut levels affect the velocity profiles of nanofluids and hybrids during the power law index number at $n = 0.4$ and $n = 1.4$ for the flow regimes in the fuzzy framework. The results illustrate that the velocity profiles are significantly impacted by the α-cut uncertainty and that hybrid nanofluids usually have higher flow performance. As the α-cut gets closer to one $(\alpha = 1)$, the velocity values of nanofluids and hybrid nanofluids converge, removing fuzzy uncertainty and validating the accurate solution.

Table 5. Fuzzy velocity profile when $R_d = 1, \theta_w = 2, Ec = 0.2, Pr = 2, Sc = 1.2, L_s = 0.5, Lb = 2$, and $Pe = 1$.

$\alpha - cut$	λ	De	Re	B	$f'(\eta, \alpha)$							
					$n < 1$				$n > 1$			
					Nanofluid $\varphi_1 = 0.04$, $\varphi_2 = 0$		Hybrid nanofluid $\varphi_1, \varphi_2 = 0.04$		Nanofluid $\varphi_1 = 0.04$, $\varphi_2 = 0$		Hybrid nanofluid $\varphi_1, \varphi_2 = 0.04$	
					$\underline{f'}$	$\overline{f'}$	$\underline{f'}$	$\overline{f'}$	$\underline{f'}$	$\overline{f'}$	$\underline{f'}$	$\overline{f'}$
0.3	0.2	1	1	0.5	0.5095	0.8614	0.4955	0.8568	0.5178	0.8698	0.5043	0.8658
			1.5		0.5112	0.8634	0.4974	0.8590	0.5230	0.8740	0.5099	0.8703
			2		0.5129	0.8652	0.4992	0.8609	0.5279	0.8775	0.5150	0.8740
	0.5	1.5	1	0.3	0.5835	0.8813	0.5659	0.5659	0.5911	0.8890	0.5742	0.8838
				0.5	0.5909	0.8805	0.5736	0.8748	0.5978	0.8883	0.5813	0.8834
				0.7	0.5963	0.8796	0.5796	0.8742	0.6029	0.8875	0.5868	0.8829
0.7	0.2	2	1		0.5845	0.7297	0.5723	0.7215	0.6017	0.7475	0.5906	0.7404
			1.5		0.5819	0.7275	0.5714	0.7207	0.6052	0.7509	0.5959	0.7452
			2		0.5857	0.7316	0.5753	0.7249	0.6135	0.7583	0.6046	0.7529
1	0.5	2	2	0.5	0.7060	0.7060	0.6931	0.6931	0.7254	0.7254	0.7144	0.7144

Table 6 examines the impact of Ec, Pr, R_d, θ_w, and α-cut levels on nanofluid and hybrid temperature profiles during the power law index number at $n = 0.4$ and $n = 1.4$ for the flow circumstances using fuzzy logic. The results show that hybrid nanofluids outperform pure ones thermally. As uncertainty lowers and α-cut approaches unity ($\alpha = 1$), both fluids temperature values converge, indicating compatibility with the crisp solution.

Table 6. Fuzzy temperature profile when $B_0 = 0.5, \lambda = 0.2, De = 1, Re = 1, Sc = 1.2, L_s = 0.5, Lb = 2$, and $Pe = 1$.

$\alpha - cut$	R_d	θ_w	Ec	Pr	$\theta(\eta, \alpha)$							
					$n < 1$				$n > 1$			
					Nanofluid $\varphi_1 = 0.04$, $\varphi_2 = 0$		Hybrid nanofluid $\varphi_1, \varphi_2 = 0.04$		Nanofluid $\varphi_1 = 0.04$, $\varphi_2 = 0$		Hybrid nanofluid $\varphi_1, \varphi_2 = 0.04$	
					$\underline{f'}$	$\overline{f'}$	$\underline{f'}$	$\overline{f'}$	$\underline{f'}$	$\overline{f'}$	$\underline{f'}$	$\overline{f'}$
0.3	1	2	0.2	2	0.6257	0.6902	0.6261	0.6952	0.6261	0.6955	0.6266	0.7007
		2.5			0.6242	0.6820	0.6247	0.6864	0.6247	0.6871	0.6252	0.6918
		3			0.6228	0.6744	0.6232	0.6783	0.6233	0.6795	0.6238	0.6836
			0.3		0.6190	0.6576	0.6204	0.6656	0.6194	0.6628	0.6209	0.6712
			0.5	2	0.6114	0.6245	0.6147	0.6405	0.6116	0.6300	0.6150	0.6464
				3	0.7096	0.7630	0.7144	0.7879	0.7096	0.7699	0.7145	0.7950
				4	0.7750	0.8631	0.7807	0.8956	0.7748	0.8712	0.7807	0.9039
0.7	2	2	0.2	2	0.5384	0.5467	0.5382	0.5472	0.5395	0.5493	0.5394	0.5501
		2.5			0.5336	0.5385	0.5332	0.5388	0.5347	0.5411	0.5345	0.5416
		3	0.2		0.5310	0.5289	0.5285	0.5310	0.5301	0.5336	0.5297	0.5339
			0.3	2	0.5246	0.5237	0.5253	0.5255	0.5257	0.5262	0.5264	0.5283
				3	0.6446	0.6587	0.6468	0.6630	0.6456	0.6615	0.6479	0.6661
1	3	2	0.2	2	0.4620	0.4620	0.4615	0.4615	0.4636	0.4636	0.4632	0.4632

Table 7 displays concentration profiles of nanofluids and hybrids under the power law index number at $n = 0.4$ and $n = 1.4$ of the flow conditions, illustrating the impact of Schmidt number (Sc), homogeneous-heterogeneous reaction parameter (Ls), and α-cut levels using fuzzy logic. Hybrid nanofluids improve concentration regardless of parameters. As the α-cut approaches unity ($\alpha = 1$), both fluid concentration values match the deterministic solution with certainty.

Table 7. Fuzzy concentration profile when $B_0 = 0.5, \lambda = 0.2, De = 1, Re = 1,$ when $R_d = 1, \theta_w = 2, Ec = 0.2, Pr = 2, Lb = 2,$ and $Pe = 1$.

$\alpha - cut$	Sc	Ls	$m(\eta, \alpha)$							
			$n < 1$				$n > 1$			
			Nanofluid $\varphi_1 = 0.04, \varphi_2 = 0$		Hybrid nanofluid $\varphi_1, \varphi_2 = 0.04$		Nanofluid $\varphi_1 = 0.04, \varphi_2 = 0$		Hybrid nanofluid $\varphi_1, \varphi_2 = 0.04$	
			$\underline{f}'$	$\overline{f}'$	$\underline{f}'$	$\overline{f}'$	$\underline{f}'$	$\overline{f}'$	$\underline{f}'$	$\overline{f}'$
0.3	1.2	0.5	1.8828	1.8046	1.8786	1.8036	1.8852	1.8076	1.8811	1.8068
		0.8	1.4991	1.2334	1.4970	1.2332	1.5005	1.2357	1.4985	1.2357
		1	1.3220	1.0278	1.3208	1.0281	1.3230	1.0296	1.3219	1.0300
0.7	1.5	0.5	1.9184	1.8035	1.9147	1.8009	1.9216	1.8079	1.9182	1.8057
		1	1.2796	1.1271	1.2789	1.1270	1.2808	1.1288	1.2802	1.1289
1	1.5	1	1.2024	1.2024	1.2020	1.2020	1.2039	1.2039	1.2036	1.2036

The impacts of the bioconvection Lb, Pe, and α-cut levels on motile microbe profiles in nanofluids and hybrids with the power law index number at $n = 0.4$ and $n = 1.4$ for the flow regimes are explored in **Table 8** using fuzzy logic. Under various conditions, hybrid nanofluids had more microorganisms than their equivalents. The microbe numbers in both fluids match when the α-cut is one (α = 1), confirming the accuracy of the deterministic solution.

Table 8. Fuzzy microorganism profile when $B_0 = 0.5, \lambda = 0.2, De = 1, Re = 1,$ when $R_d = 1, \theta_w = 2, Ec = 0.2, Pr = 2$.

$\alpha - cut$	Lb	Pe	$\chi(\eta, \alpha)$							
			$n < 1$				$n > 1$			
			Nanofluid $\varphi_1 = 0.04, \varphi_2 = 0$		Hybrid nanofluid $\varphi_1, \varphi_2 = 0.04$		Nanofluid $\varphi_1 = 0.04, \varphi_2 = 0$		Hybrid nanofluid $\varphi_1, \varphi_2 = 0.04$	
			$\underline{f}'$	$\overline{f}'$	$\underline{f}'$	$\overline{f}'$	$\underline{f}'$	$\overline{f}'$	$\underline{f}'$	$\overline{f}'$
0.3	2	1	0.4480	0.2618	0.4428	0.2486	0.4502	0.2718	0.4451	0.2593
		2	0.8873	0.4018	0.9413	0.4247	0.8679	0.3913	0.9204	0.4132
		3	4.1147	0.9896	3.9830	1.0260	4.1614	0.9822	4.0266	1.0177
0.7	2	1	0.4021	0.3103	0.3941	0.2983	0.4061	0.3182	0.3984	0.3069
		2	0.8377	0.5907	0.8833	0.6202	0.8184	0.5763	0.8625	0.6047
1	3	1	0.6753	0.6753	0.6682	0.6682	0.6800	0.6800	0.6733	0.6733

9. Conclusion

The present investigation studied microorganisms, temperature, concentration, and membrane profiles in the radiative magnetohydrodynamic flow of a Sutterby hybrid nanofluid over a stretching sheet using homogeneous-heterogeneous processes and Buongiorno's nanomaterial model. This work uses MATLAB to translate the governing equations into nonlinear ordinary differential equations to investigate nanofluid and hybrid nanofluid thermal and flow properties affected by magnetic, radiative, and convective influences. The primary objective was to comprehend how hybrid nanoparticles might diminish thermal radiation penetration and improve thermal management in engineering and biological systems. The principal conclusions are outlined below:

- Velocity increases with the Deborah number (De), Reynolds number (Re) and velocity ratio parameter (λ) and velocity slip parameter (c_1), but magnetic field intensity diminishes fluid motion.

- Temperature rises with increasing Eckert number (Ec), thermal radiation parameter (R_d), Brownian motion parameter (Nb) and thermophoretic parameter (Nt), while it decreases with higher temperature ratio (θ_w) and temperature slip parameter (c_2).
- The nanoparticle concentration profile increases when the Schmidt number (Sc), the homogeneous and heterogeneous parameters(Ls) and the concentration slip parameter (c_3) increases.
- The microorganism profile increases with the Peclet number (Pe) and microorganism slip parameter (c_4), but decreases with the Lewis number (Lb) indicating enhanced bioconvection behavior of fluid flow.
- Fuzzy analysis shows stable, consistent physical results at $\alpha = 1$, demonstrating the robustness of fuzzy modeling for systems with uncertainty in nanoparticle volume fraction.

Advantages of the proposed work are

- The model incorporates various physical phenomena (MHD, nonlinear radiation, homogeneous–heterogeneous interactions, bioconvection, and non-Newtonian Sutterby fluid) under a singular cohesive framework, which are infrequently considered together.
- The FST attains strong and dependable value than crisp value in apprehending incertitude in nanoparticle volume fractions.
- Nonlinear ODE numerically solved by BVP using MATLAB bvp5c yields reliable outputs, both numerical and graphical.

Limitations of the proposed work are

- The analysis is limited to steady, 2D laminar flow and excludes independent-of-time, turbulent flow and 3D geometry like cone, wedge, and cylinder effects.
- Uncertainty is modeled only using TFN; other fuzzy uncertainty models are not prospected
- This study is entirely numerical and graphical, lacking any experimental or real-world endorsements.

Future studies may investigate time-dependent flow in cylindrical geometries, explore different types of nanoparticles for specific applications, develop fuzzy concepts into fuzzy topological concepts, and adapt solution methods to other shooting methods.

Conflicts of Interest

The authors confirm that there is no conflict of interest to declare for this publication.

Acknowledgments

The authors would like to express their gratitude to Government College Technology, Coimbatore and Government College of Engineering, Erode, India.

AI Disclosure

During the preparation of this work, the author(s) used generative AI in order to improve the language of the article. After using this tool or service, the author(s) reviewed and edited the content as needed and took full responsibility for the publication.

References

Aldabesh, A., Haredy, A., Al-Khaled, K., Khan, S.U., & Tlili, I. (2022). Darcy resistance flow of Sutterby nanofluid with microorganisms with applications of nano-biofuel cells. *Scientific Reports*, *12*(1), 7514. https://doi.org/10.1038/s41598-022-11528-7.

Asaigeethan, P., Vaithiyalingam, K., Loganathan, K., Prabu, K., Abbas, M., & Mishra, N.K. (2024). Numerical study of Carreau fuzzy nanofluid across a stretching cylinder using a modified version of Buongiorno's nanofluid model. *Alexandria Engineering Journal*, *101*, 318-329.

Asjad, M.I., Zahid, M., Jarad, F., & Alsharif, A.M. (2022). Bioconvection flow of MHD viscous nanofluid in the presence of chemical reaction and activation energy. *Mathematical Problems in Engineering*, *2022*(1), 1707894.

Awan, A.U., Shah, S.A.A., & Ali, B. (2022). Bio-convection effects on Williamson nanofluid flow with exponential heat source and motile microorganism over a stretching sheet. *Chinese Journal of Physics*, *77*, 2795-2810.

Barhoi, A., Hazarika, G.C., & Dutta, P. (2018). Numerical study of fuzzified boundary value problem for Couette type flow of fluid mechanics. *Annals of Pure and Applied Mathematics*, *16*(2), 373-384.

Basit, M.A., Imran, M., Khan, S.A., Alhushaybari, A., Sadat, R., & Ali, M.R. (2023). Partial differential equations modeling of bio-convective sutterby nanofluid flow through paraboloid surface. *Scientific Reports*, *13*(1), 6152. https://doi.org/10.1038/s41598-023-32902-z.

Biswal, U., Chakraverty, S., & Ojha, B.K. (2020). Natural convection of nanofluid flow between two vertical flat plates with imprecise parameter. *Coupled Systems Mechanics*, *9*(3), 219-235.

Dash, R.K., Mishra, S.R., & Pattnaik, P.K. (2022). Influence of radiative heat energy on the MHD flow of Cu-kerosene nanofluid over a vertical plate: Laplace transform technique. *Biointerface Research in Applied Chemistry*, *12*(5), 6234-6251.

Dubois, D., & Prade, H. (1978). Operations on fuzzy numbers. *International Journal of Systems Science*, *9*(6), 613-626.

Farooq, U., Jan, A., Hilali, S.O., Alhagyan, M., & Gargouri, A. (2024). Bioconvection study of MHD hybrid nanofluid flow along a linear stretching sheet with Buoyancy effects: local non-similarity method. *International Journal of Heat and Fluid Flow*, *107*, 109350. https://doi.org/10.1016/j.ijheatfluidflow.2024.109350.

Gorla, R.S.R., Chamkha, A., & Rashad, A.M. (2010). Mixed convective boundary layer flow over a vertical wedge embedded in a porous medium saturated with a nanofluid. In *2010 3rd International Conference on Thermal Issues in Emerging Technologies Theory and Applications* (pp. 445-451). IEEE. Cairo, Egypt.

Hamid, A., Mehtab, U., & Farooq, N. (2025). Computational analysis for bioconvection flow of nanofluid along a bidirectional surface containing gyrotactic microorganisms embedded in a Darcy-Forchheimer porous medium. *International Journal of Thermofluids*, *26*, 101059. https://doi.org/10.1016/j.ijft.2025.101059.

Imran, M., Kamran, T., Khan, S. A., Muhammad, T., & Waqas, H. (2022). Physical attributes of bio-convection in nanofluid flow through a paraboloid of revolution on horizontal surface with motile microorganisms. *International Communications in Heat and Mass Transfer*, *133*, 105947. https://doi.org/10.1016/j.icheatmasstransfer.2022.105947.

Khan, M.N., Ahmad, S., Alrihieli, H.F., Wang, Z., Hussien, M.A., & Afikuzzaman, M. (2023). Theoretical study on thermal efficiencies of Sutterby ternary-hybrid nanofluids with surface catalyzed reactions over a bidirectional expanding surface. *Journal of Molecular Liquids*, *391*, 123412. https://doi.org/10.1016/j.molliq.2023.123412.

Khan, S.A., Waqas, H., Naqvi, S.M.R.S., Alghamdi, M., & Al-Mdallal, Q. (2021). Cattaneo-Christov double diffusions theories with bio-convection in nanofluid flow to enhance the efficiency of nanoparticles diffusion. *Case Studies in Thermal Engineering*, *26*, 101017. https://doi.org/10.1016/j.csite.2021.101017.

Mohamed, E.M., Nasr, E.H., Ahmed, K.K., Emadifar, H., Ahmed, H.M., & Alkhatib, S. (2025). Hybrid nanofluids and bioconvection: insights into bacterial behavior and particle interaction. *Boundary Value Problems*, *2025*(1), 31. https://doi.org/10.1186/s13661-025-02025-7.

Mondal, S., & Pal, D. (2024). Exploring convective entropy optimization and activation energy impact on magneto-nanofluid flow over a vertical stretched plate with Hall current and nonlinear thermal radiation using SQLM. *Hybrid Advances*, *7*, 100294. https://doi.org/10.1016/j.hybadv.2024.100294.

Mushtaq, A., Mustafa, M., Hayat, T., & Alsaedi, A. (2014). Nonlinear radiative heat transfer in the flow of nanofluid due to solar energy: a numerical study. *Journal of the Taiwan Institute of Chemical Engineers*, *45*(4), 1176-1183.

Patil, P.M., & Goudar, B. (2023). Entropy generation analysis from the time-dependent quadratic combined convective flow with multiple diffusions and nonlinear thermal radiation. *Chinese Journal of Chemical Engineering*, *53*, 46-55.

Rahman, M., Haq, F., Ijaz Khan, M., Awwad, F.A., & Ismail, E.A. (2023). Numerical assessment of irreversibility in radiated Sutterby nanofluid flow with activation energy and Darcy Forchheimer. *Scientific Reports*, *13*(1), 18982. https://doi.org/10.1038/s41598-023-46439-8.

Ramesh, G.K., Madhukesh, J.K., Aly, E.H., & Pop, I. (2022). Modified Buongiorno's model for biomagnetic hybrid nanoliquid past a permeable moving thin needle. *International Journal of Numerical Methods for Heat & Fluid Flow*, *32*(11), 3551-3578.

Sabir, Z., Imran, A., Umar, M., Zeb, M., Shoaib, M., & Raja, M.A.Z. (2021). A numerical approach for 2-D Sutterby fluid-flow bounded at a stagnation point with an inclined magnetic field and thermal radiation impacts. *Thermal Science*, *25*(3 Part A), 1975-1987.

Seikkala, S. (1987). On the fuzzy initial value problem. *Fuzzy Sets and Systems*, *24*(3), 319-330.

Shaw, S., Samantaray, S.S., Misra, A., Nayak, M.K., & Makinde, O.D. (2022). Hydromagnetic flow and thermal interpretations of Cross hybrid nanofluid influenced by linear, nonlinear and quadratic thermal radiations for any Prandtl number. *International Communications in Heat and Mass Transfer*, *130*, 105816. https://doi.org/10.1016/j.icheatmasstransfer.2021.105816.

Upreti, H., Joshi, N., Pandey, A.K., & Rawat, S.K. (2022). Homogeneous–heterogeneous reactions within magnetic sisko nanofluid flow through stretching sheet due to convective conditions using Buongiorno's model. *Journal of Nanofluids*, *11*(5), 646-656.

Vaidya, H., Choudhari, R., Mebarek-Oudina, F., Animasaun, I.L., Prasad, K.V., & Makinde, O.D. (2021). Combined effects of homogeneous and heterogeneous reactions on peristalsis of Ree-Eyring liquid: application in hemodynamic flow. *Heat Transfer*, *50*(3), 2592-2609.

Zeeshan, A., Awais, M., Alzahrani, F., & Shehzad, N. (2021). Energy analysis of non-Newtonian nanofluid flow over parabola of revolution on the horizontal surface with catalytic chemical reaction. *Heat Transfer*, *50*(6), 6189-6209.

Zulqarnain, R.M., Nadeem, M., Siddique, I., Samar, M., Khan, I., & Mohamed, A. (2023). Numerical study of second-grade fuzzy hybrid nanofluid flow over the exponentially permeable stretching/shrinking surface. *Frontiers in Physics*, *11*, 1301453. https://doi.org/10.3389/fphy.2023.1301453.